https://doi.org/10.5194/egusphere-2026-4034
Preprint. Discussion started: 27 July 2026

QuSI-DEM version 1.0: A polygon-based discrete element sea ice model in spherical coordinates. Part I: Model description

Scott M. Durski [1], Jennifer K. Hutchings [1], Adam Bateson [2], Anton Kulchitsky [3], and Gleb Velikhovskiy [4]

[1]College of Earth Ocean and Atmospheric Sciences, Oregon State University, Corvallis, OR, USA
[2]University of Reading, Whiteknights, Reading, RG6 6AH, England
[3]Progresstech Group LLC, Houston, TX, USA
[4]Rapid Operational Response Unit KORD (Rifle Infantry) of Kyiv Region, National Police of Ukraine, Kyiv, Ukraine

Correspondence: Scott M. Durski (durskis@oregonstate.edu)

Abstract. Discrete element modeling (DEM) provides a methodology for simulating the dynamics of sea ice from fracture through post-failure granular behavior. Because the approach is designed explicitly to represent the cohesive or frictional forces between distinct floes, it may offer a better representation than continuum-based approaches for some phenomena. As such, discrete element models (DEMs) provide a complementary approach to sea ice modeling at geophysical scales. However, many uncertainties remain regarding best practices in the application of the method. These range from choosing element shape, element scale, contact physics, and numerical implementation. Here we describe a novel polygon-based discrete element sea ice model, developed with careful attention to the implementation details and the fundamental response of interacting element-pairs. The crack patterns that develop as a result of sea ice fracture depend critically on the elastic and dissipative response of the material. Propagation of cracks can depend as much on the characteristics of post-failure element contacts as intact ones. So, distinct parameters are introduced to the contact physics in this model to provide control of the failure rate and timing of transitions in contact response and to constrain the amount of energy and momentum transfer in the contact failure process. Stresses can be communicated over great distances in sea ice due to its rigidity. This can present difficulty in specifying boundary conditions for simulations of localized processes as remote influences may be large. With this in mind, other like other models in its class, this model is formulated in spherical coordinates, and borrows from finite element mesh generation and refinement techniques that make it possible to simulate across scales up to the planetary without excessive computational cost.

https://doi.org/10.5194/egusphere-2026-4034
Preprint. Discussion started: 27 July 2026

1 Introduction

The bulk properties of granular assemblies can be difficult to accurately represent with continuum approximations because the dynamics depend intrinsically on the characteristics of individual grains and grain contacts. In sea ice, at geophysical scales, this can manifest as anisotropy in pack ice strength that arises from large scale fracture patterns with preferred orientations (Hibler and Schulson, 2000). The discrete element method (DEM) was first developed by Cundall and Strack (1979) to represent granular materials in rock mechanics, where similar anisotropy can exist. They found they could accurately represent the evolution of the force distribution within an assemblage, by distinctly representing each element (or grain) in a Lagrangian frame, computing the forces between elements and numerically integrating to update particle positions. Mark Hopkins first implemented this method for problems involving sea ice, using it to represent sea ice ridging processes (Hopkins, 1994) and pack ice dynamics (Hopkins and Thorndike, 2006).

The method has been useful in exploring the physical response of pack ice to loading from winds (Hopkins et al., 2004; Wilchinsky and Feltham, 2011) , waves (Herman, 2017), and oceanic eddies (Moncada et al., 2025) in idealized case studies. In recent years, there is interest in extending the DEM approach to simulate sea ice in realistic situations and capture observed phenomena. West et al. (2022) and Tsarau et al. (2024) use sea ice DEM models to reproduce the location and characteristics of ice arches over straits. Turner et al. (2022) has worked toward implementation in climate models, while Tsarau et al. (2024) has explored how ice drift and deformation may be well-captured by a DEM where coastlines contribute geometrically complex boundary conditions.

Discrete element models however are far from monolithic in their formulation. Three-dimensional elements have been used for the most fine scale problems, such as those representing laboratory-scale samples of sea ice (Khosravi et al., 2026), sea ice structure interaction (Chen and Pei, 2025; Dong et al., 2025), or ridging processes (Åström and Polojärvi, 2024). Two-dimensional sea ice DEM models are more common for geophysical scale phenomena as the aspect ratio diminishes the relevance of the vertical dimension, other than for processes that can be parameterized such as ridging/rafting or thermal cracking. In two-dimensional DEM, circular elements have been used in some cases (Turner et al., 2022; Herman, 2016), leveraging the symmetry of the element shape for computational benefit and often building off models already established for molecular modeling. However, pack ice being a quasi-brittle material, initially forms angular irregular shaped ice floes on break up, with these only becoming rounded through melt and frictional processes in floe interaction, ridging and shearing. It has been shown that floe geometry is important in the response of ice floe drift to ocean currents (Brenner et al., 2023) because it plays a significant role in determining the shear stresses at the floe edges. These irregular shaped floes can be more accurately represented, and with fewer, polygonal elements than with circular ones. It is perhaps for this reason that the foundational sea ice DEM work used convex polygonal elements (Hopkins, 1996; Hopkins et al., 2004; Wilchinsky and Feltham, 2011; Hopkins, 2002). An advantage of polygons is that they can fully fill a space to represent 100% ice coverage. The flat abutting edges they provide more realistically match those typically found providing more accurate representation of the interactions between floes. Disk shaped elements, which contact each other along curved edges, must make special accommodations for rolling resistance. Some of the most recent work has extended polygonal formulations to allow for element break up into

https://doi.org/10.5194/egusphere-2026-4034
Preprint. Discussion started: 27 July 2026

smaller, potentially concave polygonal elements, such as in the Subzero model of Montemuro and Manucharyan (2023) and the Level Set Discrete Element Method for Sea Ice by Moncada et al. (2023).

Sea ice in general can be characterized as brittle and stiff. Cracks propagate as the medium adjusts to an initial failure event through the propagation of elastic waves. So models aimed at reproducing cracking patterns need to either resolve or parameterize the dynamics in the material at a very fine temporal scale. This creates a computational constraint in DEM that compounds the usual limitations spatial resolution commonly causes in geophysical modeling. With increasing computational resources, efforts to optimize and parallelize discrete element models will allow us to extend the range of scales over which we can model sea ice by simply increasing the number of interacting elements, as demonstrated by Åström and Polojärvi (2024). However, depending on the scales of interest, contact physics describing element interactions represents physical processes that need to be treated in different ways. For elements of meters to tens of meters, elements are directly involved in ridging processes, which should be described as the frictional process of block sliding and work against gravity and buoyancy. Larger elements must parameterize ridging that might occur along element edges, for example, as Hopkins et al. (2004) did by using results from Hopkins (1994) to parameterize ridging. Sea ice experiences cracking at all scales. In DEMs, this can be represented as bonds between elements breaking or breakup of elements (in some models). The stresses leading to bond breaking will differ depending on the scale resolved, either due to the size effect Bažant (2001) or because the underlying structure controlling the sea ice strength differs at the different scales (following Lynmcnutt and Overland (2003)).

The particular challenge of discrete element modeling is to accurately represent the internal stresses in a floe consisting of a set of bonded element, capture the location and timing of bond failures that lead to crack propagation and breakup into smaller floes, and then also correctly represent the characteristics of those smaller floes and their interactions. Often the contact physics that is applied is based on a combination of the phenomenology, i.e. the normal force between elements should be a function of the area of overlap between them, and numerical necessity, i.e. viscous damping at a contact to prevent rapid element acceleration due to force imbalance created at instant of bond failure. Contacts are represented by springs, beams, dashpot and ratchets that approximate the physics. But the emphasis in most DEM studies is on capturing emergent bulk characteristics of the system, such as floe size distribution or ridging patterns. Less work has focused on determining DEM numerical accuracy, ensuring energy conservation in collisions or understanding how the specific contact parameterizations affect the overall solution.

In this paper, we describe the Quaternion-based Sea Ice DEM (QuSI-DEM), first prototyped as 'Siku' in Kulchitsky et al. (2016), for the study of pack ice mechanics. The model adopts some of the more traditional aspects of sea ice DEMS, like using two-dimensional convex polygonal elements and failure criteria based on the approximated stress at the element interfaces Hopkins and Thorndike (2006); Wilchinsky and Feltham (2011). But we take a top-down approach to consider how a DEM might be developed for regional to basin scale application without excessive computational cost. With this in mind, unlike previous sea ice DEMs that utilize a Cartesian approximation, we solve for the floe dynamics on the surface of a sphere, using unit quaternions to describe element positions. In the exposition of the model description, particular attention is focused on the formulation for the transition in the contact physics at bond failure and on post-failure contact characteristics with recognition

https://doi.org/10.5194/egusphere-2026-4034
Preprint. Discussion started: 27 July 2026

that crack propagation depends critically on the relative fractions of energy and momentum dissipated locally versus propagated away.

In the next section the physical model formulation for QuSI-DEM is described, including forces in the momentum balance on each element, how contact between elements is handled and lateral boundary conditions. This is followed by a detailed discussion of how transitions in contact physics are represented in the model in Sect. 3. The implementation in spherical coordinates and details of the numerical methods used to solve for the sea ice evolution are discussed in Sect. 4. Finally the tools that have been developed to create initial element distributions for regional to basin scale domains with mesh refinement to allow for enhanced resolution in select areas are discussed in Sect. 5.

This article is part one of a two-part exposition on QuSI-DEM . Part II is focused on a model evaluation, demonstrating the functionality of various parameters at the contact level, in highly idealized simulations and showing the sensitivity of the solution to contact physics parameters in a realistic case study of sea ice dynamics at Bering Strait. Throughout the model description that follows, references to relevant sections of the Part II paper will be labeled with 'II-' prepended to section identifiers.

2 Model Formulation

QuSI-DEM is designed to simulate the motion of ice on the surface of a sphere subject to atmospheric and oceanic drag forces, boundary forcing, and internal ice stress. The ice is discretized as elements that may initially be bonded as large floes or sheets. Fracture along the edges of the bonded elements is modeled to simulate cracking of consolidated pack ice. When bonds break due to accumulated damage along an edge, leads can open up between elements, or they may remain in frictional contact, interacting as a granular flow. Sea ice thermodynamics is not incorporated, as the focus of the model is mechanical processes of pack ice failure and flow over timescales of minutes to days. The spherical geometry of the model opens the possibility of studying not only local and regional ice mechanics but also planetary scale deformation processes on, for example, an icy moon.

Model domains consist of partially or fully ice covered regions, along with fixed, or movable boundary elements. Ice elements are restricted to being convex polygons mapped to the sphere, but can vary in shape, size, and number of vertices. Ice dynamics is simulated on the surface of the sphere; flexure or failure normal to the sphere surface is not currently considered.

2.1 Model algorithm

We start by describing the model algorithm as depicted in Figure 1. At model initialization, element shapes and initial positions are read from files that specify vertex positions on the sphere, element connectivity, and element type (1). Elements may be identified as ice, coastline, or control element, or subsets of ice elements may be labeled as belonging to a particular group or floe. Optionally, initial velocities and/or rate of rotation can be specified for element. Initial bonds between elements are identifed based on close proximity of vertex pairs (2) unless elements are otherwise labeled.

https://doi.org/10.5194/egusphere-2026-4034
Preprint. Discussion started: 27 July 2026

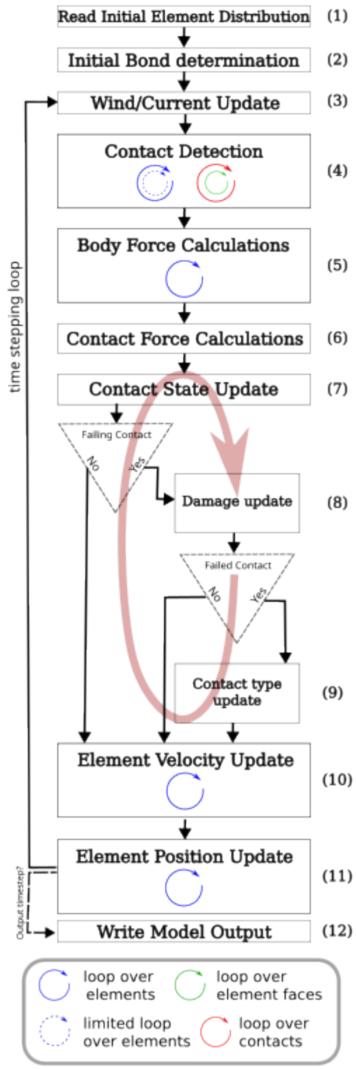

Figure 1. Flow chart of numerical model implementation

At the start of each time step, the model updates the gridded wind and current speed fields, linearly interpolating between time records and reading in new records as required (3). Following this, new element contacts are detected in two stages (4). Potential new contacts are first identified by considering the overlap of disks that encompass each element, where the radius r_e of the disk is slightly larger than the distance between the element centroid and its farthest vertex. Any pair of elements for

https://doi.org/10.5194/egusphere-2026-4034
Preprint. Discussion started: 27 July 2026

which the distance between the centroids is less than $r_{e_1} + r_{e_2}$ are considered potentially in contact. To reduce the number of distance comparisons in this first step, elements are first sorted by longitude and only element-disks that intersect in longitude are checked for latitudinal overlap. Each identified potential contact pair, that is not already identified as a bond, is then mapped onto a shared Cartesian plane (see Sect. 4.3 below) and collision contact is determined to occur if there is an area of overlap between the two polygons. Determining this amounts to a search for multiple line segment intersections, which can be one of the most computationally intensive portions of the model algorithm. Once collision contacts have been determined, they are added to a list of joint (bonded) contacts.

Body forces on the elements are calculated next (5). Bilinear interpolations are used to determine the field values at the centroid of each element on each time step. Then the wind and ocean stresses on the elements are calculated from 10 m wind speed and ocean near-surface velocity. The Coriolis force on each element is calculated from the latitude of the centroid and the element velocity. Wind and water turning angles may also be applied in this step if appropriate.

After all body forces on the elements have been calculated, the contact forces and torques between elements are calculated (6). These include those due to elastic compression, tension and shear, viscous contact damping, and friction. After all contact forces associated with a contact have been calculated and accumulated (7), the stresses at the contact are compared against failure criteria. If they exceed a criterion, the damage to the contact increases (8). If the damage exceeds the maximum threshold, the contact fails and may be reclassified as a collision contact if the previous contact type were a bond that failed in pure compression or shear under compression (9).

With all forces and torques on each element accumulated, accelerations are calculated, angular velocities on the sphere are updated with an Euler time step (10), and finally element quaternion coordinates are updated using the time-stepped velocities and element rotation rates (11). At save intervals, model output is written to HDF5 format files, with the option for saving extensive element-based and contact-based fields (12).

The numerical model described above has been coded in C++ with embedded Python. The embedded python provides a more accessible interface for specifying the model setup and extracting diagnostics while the model is running. Currently, the code is serial, but given the discrete nature of virtually all the calculations in the time stepping loop, it is expected that parallelization will be straightforward. For the scale of problems considered up to this point, running ensembles of serial computations simultaneously has proven a practical alternative to code parallelization.

2.2 Forces and torques on an element

Elements can be subject to distributed forces, such as wind stress, water stress, and Coriolis force, along with contact forces associated with bonds or collisions between elements. For simplicity, we start by describing the forces on each element in a Cartesian frame. The transformation to the surface of a sphere will be presented in Sect. 4.1. The force on the center of mass of an element in an inertial cartesian x-y plane can be written as

$$\mathbf{F}_{\mathrm{e}} = \mathbf{F}_{\mathbf{d.atm}} + \mathbf{F}_{\mathbf{d.ocn}} + \mathbf{F}_{\mathbf{Cor}} + \mathbf{F}_{\mathbf{slope}} + \sum_{i=1}^{\mathbf{N_c}} \mathbf{F}^{i}_{\mathbf{b,c}}, \tag{1}$$

https://doi.org/10.5194/egusphere-2026-4034
Preprint. Discussion started: 27 July 2026

where $\mathbf{F}_{\mathrm{e}}$ is the total force on the element in the x-y plane, $\mathbf{F}_{d.atm}$ and $\mathbf{F}_{d.ocn}$ are the air-ice and ocean-ice drag forces respectively, $\mathbf{F}_{Cor}$ is the Coriolis force, $\mathbf{F}_{slope}$ accounts for the sea surface slope and $\mathbf{F}^{i}_{\mathbf{b,c}}$ signifies the contact force (bond or collision) with the i-th neighboring element (where N_c is the number of contacts). Bold text in the equations here, denotes vector quantities. Each element also experiences torques. At present we do not consider gradients in ocean or atmospheric drag to induce torques. So, the total torque on an element can be described as

$$\mathbf{T}_{\mathrm{e}} = \sum_{\mathbf{i=1}}^{\mathbf{N_c}} \mathbf{F}^{i}_{\mathbf{b,c}} \times \mathbf{r}_i. \tag{2}$$

In this equation r_i is the radial distance from the centroid of the element to the point of application of the contact force. For example, this is the mid-point of a polygon side for a bonded contact with a neighboring element.

Wind and ocean drag forces are specified using a quadratic function of relative velocity:

$$\mathbf{F_d} = A_e C_d |\tilde{\mathbf{W}} - \mathbf{V_e}|(\tilde{\mathbf{W}} - \mathbf{V_e}), \tag{3}$$

where A_e is the horizontal element area, C_d is the drag coefficient, $\tilde{\mathbf{W}}$ is the wind or ocean current velocity at the element centered specified at a reference height above or below the interface and $\mathbf{V_e}$ is the velocity of the ice element. A wind or water turning angle can also be applied in the model to account for wind or current forcing data located some distance from the surface. In this case, a fixed rotation can be applied to the orientation of the wind or current vector.

The Coriolis force on the element is specified as,

$$\mathbf{F_{Cor}} = m_e \cdot f\hat{\mathbf{k}} \times \mathbf{V}_e, \tag{4}$$

where m_e is the mass of the element and f is the Coriolis parameter ($2\Omega_e sin\phi$, where Ω_e is the planetary rotation rate and ϕ is the latitude). $\mathbf{V}_e$ is the horizontal velocity vector (v_x, v_y) in the Cartesian frame at the element centroid. This term can be effectively turned off in the model by increasing the period of rotation of the planet Ω_e to a very large value.

The gravitational force associated with acceleration down the sea surface slope gradient is calculated as

$$\mathbf{F_{slope}} = -m_e g \nabla \mathrm{H_o}, \tag{5}$$

where g is the gravitational acceleration at the planetary surface and $\mathrm{H_o}$ is the sea surface gradient at the location of the center of mass of the element.

2.3 Bonds

In order to model sea ice failure, in which a sheet of ice fractures into smaller interacting floes, it is necessary to provide contact physics representative of a continuous material prior to cracking and representative of the interaction of discrete objects post-failure. Here, pre-failure contact physics is referred to as *bond physics*, and the region of contact is referred to as a *bond* or *joint*. In the model, bonded elements need to be capable of supporting tensile, shear, and compressive forces up to the desired failure criteria. Post-failure, no tensile forces or bending moments remain, but the elements still resist compression into each other, and lateral friction may provide residual shear strength.

https://doi.org/10.5194/egusphere-2026-4034
Preprint. Discussion started: 27 July 2026

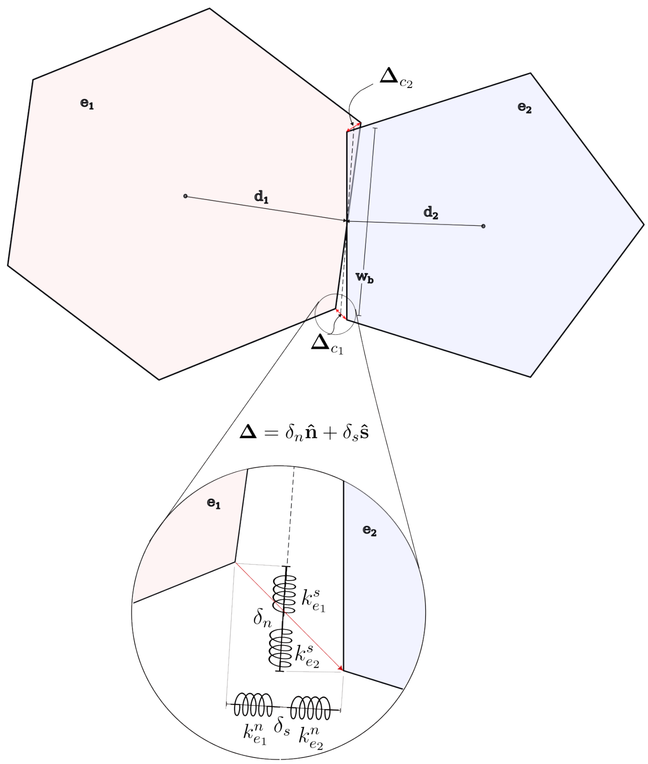

Figure 2. Diagram of the geometry of a bond contact

The model currently allows only bonds between elements that share a common side in the initial element distribution. Currently, bond physics is restricted to edges that are equal in length with initially aligned vertex pairs. Along the bonded contact, the force on each element is a linear function of the vector displacement of the associated polygon corner pairs, $\boldsymbol{\Delta}_{c_1}$ and $\boldsymbol{\Delta}_{c_2}$ (Fig. 2). The magnitude of the normal force per unit length $\mathrm{f_n}$ exerted by an element at a joint can be expressed as a function of a linear spring constant k^n or in terms of geometry and elastic modulus E

$$\mathrm{f_n} = k^n \delta_n = \frac{Eh}{d}\delta_n, \tag{6}$$

where h is the vertical thickness of the element, d is the distance from the element centroid to the midpoint of the element contacting edge and $\delta_e = \Delta \cdot \hat{\mathbf{n}}$ is the normal displacement of the joint. Similarly, the tangential force magnitude per unit length is

$$\mathrm{f_s} = k^s \delta_s = \frac{Gh}{d}\delta_s, \tag{7}$$

where G is the shear modulus of the ice and $\delta_s = \Delta \cdot \hat{\mathbf{s}}$ is the tangential displacement. Since elements associated with a bond contact can have different thicknesses or material characteristics, effective spring constants k^n_* and k^s_* need to be weighted

https://doi.org/10.5194/egusphere-2026-4034
Preprint. Discussion started: 27 July 2026

averages. This is done by considering individual springs from the two elements to be connected in serial. The effective spring constants k_* are then expressed as

$$\frac{1}{k_*} = \frac{1}{k_{e_1}} + \frac{1}{k_{e_2}}, \tag{8}$$

where k_{e_1} is the spring constant associated with the first element and k_{e_2} is that for the second. Combining Eq. (8) with Eq. (6) yields the effective normal spring constant for joints:

$$k_*^n = \frac{E_1 h_1 E_2 h_2}{E_1 h_1 d_2 + E_2 h_2 d_1}, \tag{9}$$

where the subscripts on h and d indicate the element with which they are associated. Similarly for shear,

$$k_*^s = \frac{G_1 h_1 G_2 h_2}{G_1 h_1 d_2 + G_2 h_2 d_1}. \tag{10}$$

Using the displacement of the vertex pairs that determine the joint ($\mathbf{\Delta_{v_1}}$, $\mathbf{\Delta_{v_2}}$), the average stretch of the joint is

$$\overline{\mathbf{\Delta}} = \frac{1}{2}(\mathbf{\Delta}_{v_1} + \mathbf{\Delta_{v_2}}). \tag{11}$$

The vector force per unit length $\mathbf{f_b}$ associated with this is

$$\mathbf{f^b} = k_*^n \overline{\mathbf{\Delta}} \cdot \hat{\mathbf{n}} + k_*^s \overline{\mathbf{\Delta}} \cdot \hat{\mathbf{s}}, \tag{12}$$

where $\hat{\mathbf{n}}$ and $\hat{\mathbf{s}}$ are unit normal vectors oriented in normal and shear directions. Integrating over the joint width w_b, the net elastic force applied at the center-point of the contact is

$$\mathbf{F^b_{elas}} = \int_{\mathrm{v}_1}^{\mathrm{v}_2} \mathbf{f^b} d\mathrm{w} = k_*^n \mathrm{w_b} \overline{\delta_n} \hat{\mathbf{n}} + k_*^s \mathrm{w_b} \overline{\delta_s} \hat{\mathbf{s}}. \tag{13}$$

Traditionally, polygon based discrete element sea ice models (Hopkins and Thorndike, 2006; Wilchinsky and Feltham, 2011) specify the normal direction as perpendicular to the element edge and the shear direction as tangential to it. Conceptually, this corresponds to a situation in which the joint orientations determine material characteristics. Here, as an option, we also provide the possibility of defining the normal direction as being aligned with the line connecting the center of mass of the two elements. This element-centric view, for example, applies the elastic modulus when two elements are pulled directly apart from each other irrespective of the element face orientation between them. In a joint-centric formulation, the force associated with elements being pulled directly away from each other would depend on both shear and elastic moduli. The net effect of the difference between these formulations is typically small in complex systems consisting of many elements. A demonstration of the single bond response to relative motion between elements will be presented in Part II of this manuscript in Sect. II-2.1.1. The impact of the element center-of-mass normal or contact normal orientation will be presented in Sect. II-2.2.2.

The force associated with the average displacement of the vertices described above in Eq. (13) acts to translate the center of mass of the element. Also, since the force is applied at the center of the element contact face, there will be an associated torque on the center of mass of each element, proportional to $\mathbf{d} \times \mathbf{F_b}$. The vector difference in the force associated with the

https://doi.org/10.5194/egusphere-2026-4034
Preprint. Discussion started: 27 July 2026

displacements of the polygon corners $\mathbf{\Delta_{c_1}} - \mathbf{\Delta_{c_2}}$ also contributes a force couple that provides rotational acceleration of each element center of mass about the mid-point of the bond contact.

The bond forces described above are purely elastic. An optional viscous damping term is included in the model for bonded joints with a dissipative force proportional to the relative velocity of the two elements.

$$\mathbf{F^b_{visc}} = \eta w_b^2(\mathbf{v_2} - \mathbf{v_1}), \tag{14}$$

where η is a viscosity coefficient, $\mathbf{v_1}$ and $\mathbf{v_2}$ are the velocities of the two elements.

Onset of joint failure. The normal and shear stresses at the joint are estimated from the average elastic bond force across a joint as

$$\sigma_n = \frac{\mathbf{F^b_{elas}}}{w_b h} \cdot \hat{\mathbf{n}}, \tag{15}$$

and

$$\sigma_s = \frac{\mathbf{F^b_{elas}}}{w_b h} \cdot \hat{\mathbf{s}}. \tag{16}$$

The onset of joint failure in pure compression or tension occurs when the normal stress σ_n at the contact exceeds a threshold value:

$$\sigma_n \begin{cases} > \sigma_c & \text{compressive failure,} \\ < \sigma_t & \text{tensile failure,} \end{cases} \tag{17}$$

where compressive stress is positive and tensile is negative. Shear failure occurs when the magnitude of the contact-tangential component of the stress (σ_s) exceeds the Coulomb limit such that

$$|\sigma_s| > \mu(\sigma_n - \sigma_t), \tag{18}$$

where μ is the coefficient of friction.

Joint failure in the model can be specified to occur abruptly, due to stress exceeding a failure criterion on a single time step or gradually, with joint weakening over multiple time steps, as will be presented in Sect. 3.2 below. In either case, full failure of a joint represents a fracture that extends over the length of the contact. Along that edge, tensile forces are no longer supported and shear is determined by friction between the floes rather than by displacement and properties of the intact material. A different contact physics algorithm is required at this point because the vertex pair displacement information of the bond physics is no longer an appropriate measure of the force. For example, if failure occurred in compressive shear, as depicted in Fig. 2, elastic normal forces and frictional shear forces would remain. However, the lateral displacement of vertex pairs would no longer be related to the applied forces. As the contact physics that applies in this case is considered identical to that experienced in a collision of any two unbonded elements, we refer to it here as collision physics.

https://doi.org/10.5194/egusphere-2026-4034
Preprint. Discussion started: 27 July 2026

2.4 Collisions

For collision physics, the overlap area and the geometry of the overlapping edges (Fig. 3) are used to estimate the repulsive force vector $\mathbf{F^c}$. As described in Feng et al. (2012), to ensure conservation of energy for purely elastic collisions, the functional dependence on the intersection area A_i must be chosen carefully. If the collision is purely elastic, all the kinetic energy that enters the collision must be returned to kinetic energy once the two elements are no longer in contact, regardless of the path the two elements take over the period of contact. In order to ensure this, the expression for the energy of the collision takes the form of a potential function. The orientation and position of application of the force must also conserve linear and angular momentum. Following Feng et al. (Feng et al., 2012), we use a model that satisfies the above requirements by specifying the collision force on the first element as

$$\mathbf{F^c_{elas}} = \gamma k_e^* A_i b_w \hat{\mathbf{n}}, \tag{19}$$

where A_i is the overlap area between elements and b_w is the intersection edge length (Fig. 3). $\hat{\mathbf{n}}$ is a unit vector oriented 90° counterclockwise from the vector connecting the endpoints of b_w, which is also oriented counterclockwise relative to the centroid of e_1. γ is a scaling factor introduced here for consistency between collision and bond physics that will be discussed in more detail in the following section. The location at which the collision force is applied must be on the intersection centerline determined by the geometry (b_w in Fig. 3). Here, the midpoint of b_w is used. In addition to the elastic collision force,the

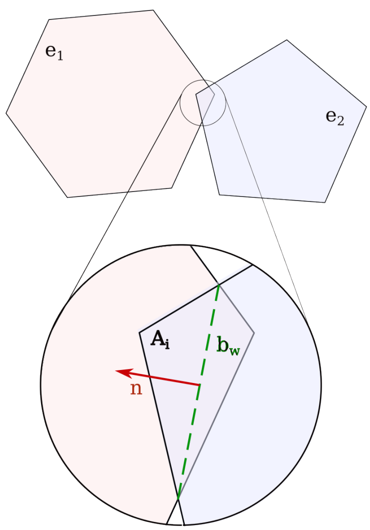

Figure 3. Diagram of the geometry of a collision contact

frictional resistance to relative motion can also be applied to elements in collision contact. Here, the maximum frictional force

https://doi.org/10.5194/egusphere-2026-4034
Preprint. Discussion started: 27 July 2026

is a function of the normal compressive force between the elements.

$$\mathbf{F^c_{maxfric}} = \lambda \mathbf{F^c_{elas}} \hat{\mathbf{b}}, \tag{20}$$

where λ is a coefficient of friction, and $\hat{\mathbf{b}}$ is a unit vector oriented in the direction of the intersection line b_w (Fig. 3). Given the finite time step, as an additional constraint, this frictional force must also not exceed the force necessary to halt the sliding between the elements.

$$\mathbf{F^c_{negate}} = min(m_1, m_2) \frac{d\mathbf{v_{12}}}{dt} \cdot \hat{\mathbf{b}}, \tag{21}$$

where m_1, m_2 indicates the mass of the two elements and v_{12} indicates their relative velocities. So, the frictional force takes the form

$$\mathbf{F^c_{fric}} = min(\mathbf{F^c_{negate}}, \mathbf{F^c_{maxfric}}). \tag{22}$$

Example of energy-conserving and frictionally damped collisions between a small set of colliding elements will be presented in Sect. II-2.1.2. A viscous damping of the normal component of collision contact is also optionally included in the model, limited in the same way as $\mathbf{F^c_{fric}}$, with a maximum value specified as

$$\mathbf{F^c_{maxvisc}} = \nu \mathbf{F^c_{elas}} \hat{\mathbf{n}}. \tag{23}$$

2.5 Lateral boundary conditions

Several options are implemented to provide lateral boundary conditions on the set of discrete ice elements. Immovable coastal elements are implemented, which can be specified to have characteristics similar or differing from the interior ice. These allow for bonding to the coast with different bond strength than for interior connections, or for free slip to emulate a situation more akin to a landfast ice edge. As described in Sect. 5, efforts are taken to create element distributions that can closely match both realistic and idealized coastlines that are not artificially corrugated due to element shape.

Some simulations require specification of a constant normal stress as a lateral boundary condition. For this situation, control elements have been implemented in the model. These otherwise unbonded elements remain permanently attached to an interior neighbor, have stress monitored at the contact, and move to reach and maintain the desired stress state. This is accomplished through a nudging term that applies a force on the element in the direction necessary to reach the desired normal stress state at the contacting face. A large viscous damping is also applied to the control element to ensure that the desired stress state can be approached nearly monotonically.

Due to the rigidity of sea ice, internal stresses can be communicated over great distances. This presents challenges for modeling even regional phenomena, as accurate lateral boundary conditions can play a critical role in the local response. As will be discussed in more detail below, one approach to alleviate the boundary condition issue is to create an initial element distribution and model domain that extends a great enough distance from the region of interest to well represent remote influences.

https://doi.org/10.5194/egusphere-2026-4034
Preprint. Discussion started: 27 July 2026

3 Transitions in contact physics

3.1 Consistency between elastic bond contact and collisions

The material properties of the sea ice elements are assumed to be consistent between bonded and unbonded elements. So, if two elements are compressed towards each other, the elastic force opposing the compression should be independent of whether the contact is bonded or in collision. However, a challenge arises because $\mathbf{F^b_{elas}}$ and $\mathbf{F^c_{elas}}$ differ in functional relationship to the geometry. This is by necessity, as bond contacts are inherently associated with relative displacement of one element face with a neighbors, whereas collisions must account for corner contacts involving multiple faces. Consistency cannot be strictly maintained with the contact model described above. To offer approximate consistency, we consider the case of pure compression of two elements with aligned edges (Fig. 4). Equating the elastic normal force between two bonded elements Eq. (13) with an identical collision contact Eq. (19), the scaling factor γ can be expressed as

$$\gamma = \frac{\overline{\delta} w_b}{A_i b_w}. \tag{24}$$

Given that A_i is approximately equal to $\overline{\delta} w_b$ and $b_w \approx w_b$, consistency between the two could be achieved if γ scales inversely with w_b, or identically, the polygon contact side length s. However, general collisions are not identified with a particular side because contact may be between corner and side, or corner and corner. b_w cannot be used for the scaling, as the form of the force would no longer be the gradient of a potential function. So, as a compromise, we choose to set the scale factor to the inverse of the average side length of the two intersecting polygons

$$\gamma = \frac{1}{\overline{s}}, \tag{25}$$

where

$$\overline{s} = \frac{1}{2}\left(\frac{s_{1_1} + s_{1_2} + ...s_{1_n}}{n_1} + \frac{s_{2_1} + s_{2_2} + ...s_{2_n}}{n_2}\right), \tag{26}$$

with the subscripts indicating the element number, the sub-subscript indicating the element side, and n indicating the number of sides of each polygon. This will ensure that if for example two bonded elements break apart in tension, then are pressed back against each other, the resistant force between the two will be comparable to if they had not been previously separated. In Sect. II-2.1.3 this formulation is demonstrated by comparing the bonded to collision response at a contact between two hexagonal elements that experiences a normal compressive force.

3.2 Joint weakening

Abrupt failure of bonds creates an unbalanced force on the associated elements that leads to rapid accelerations and transfer of stresses to the surrounding joints in the model. The subsequent force imbalance induced on neighboring elements can lead to further joint failure and crack propagation. The pattern, extent, and rate of crack propagation depend on how much of the energy stored in the joint before failure propagates away, and how much is dissipated locally. Post-failure, friction, viscous

https://doi.org/10.5194/egusphere-2026-4034
Preprint. Discussion started: 27 July 2026

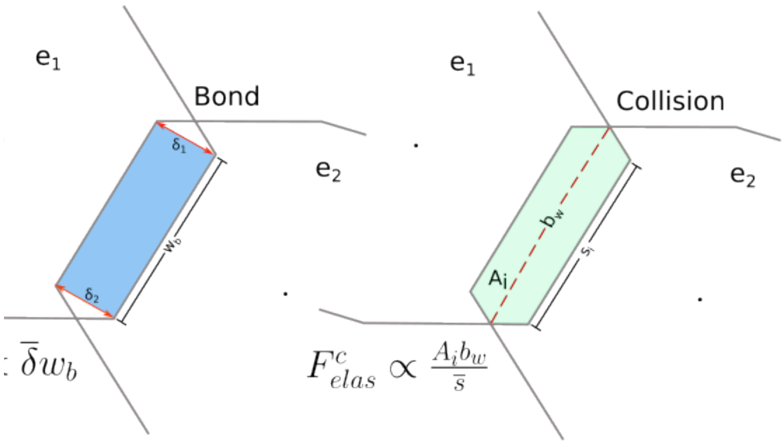

Figure 4. Diagram comparing the force associated with a bond to that of a collision

dissipation, atmospheric drag, and oceanic drag produce some local dissipation, but these represent physical processes distinct from material failure. So, in order to parameterize the inelastic aspect of joint failure, an option is included in the model to effectively dissipate the bond energy locally by allowing for a gradual weakening of the material at a contact when a failure criterion is exceeded. Joint durability D_b is degraded over time for each joint contact such that

$$\frac{dD_b}{dt} = \begin{cases} 0 & \text{for } \tilde{\sigma_t} < \sigma_n < \tilde{\sigma_c} \text{ and } \tilde{\sigma_s}| < \mu(\sigma_n - \tilde{\sigma_t}) \qquad \textit{undamaged joint}, \\ -f_r & \text{for } \sigma_n < \tilde{\sigma_t} \qquad \textit{tensile failure}, \\ -f_r \frac{\sigma_t}{\sigma_c} & \text{for } \sigma_n > \tilde{\sigma_c} \text{ or } \tilde{\sigma_s}| > \mu(\sigma_n - \tilde{\sigma_t}) \qquad \textit{compressive/shear failure}, \end{cases} \tag{27}$$

where f_r is a failure rate in seconds and the tilde refers to the modified maximum stresses as described below. D_b is assigned an initial value of 1 for all joints. It is allowed to diminish until a value D_c^o (≥ 0) is reached, at which point the contact transitions from joint to collision physics. D_b modifies the effective elastic spring constant k_e^*, and the effective shear spring constant k_s^* of the contact after the onset of failure such that

$$\tilde{k_e^*} = k_e^* D_b, \tilde{k_s^*} = k_s^* D_b, \tag{28}$$

while similarly modifying the maximum tensile, compressive, and shear strengths of the material at the joint.

$$\tilde{\sigma_t} = \sigma_t D_b, \tilde{\sigma_c} = \sigma_c D_b, \tilde{\sigma_s} = \sigma_s D_b. \tag{29}$$

The model also allows post-failure weakening of the contact, evolving D_c in a manner analogous to D_b as will be described below. The impact of varying D_b and f_r on the dynamics, stress, strain, bond and kinetic energy time series is presented inn an idealized case study involving three elements in tension, in Sect. II-2.2.1 and for three elements in compression in II-2.2.3. Note that damage is associated with a joint contact or collision contact that meets the failure criteria. Damage is not currently retained as a characteristic of an element edge for further collisions once the two elements are no longer in contact.

https://doi.org/10.5194/egusphere-2026-4034
Preprint. Discussion started: 27 July 2026

3.3 Consistency between bonded and collision contact physics under compression with weakening

In Sect. 3.1 above, the collision contact physics formulation was modified to ensure that undamaged elements that collide respond in a manner that is largely consistent with a similar bonded interaction between identical elements. A more critical situation arises when elements fail under compressive loading. Post failure, both the contact force and contact elastic energy based on the collision physics formulation (Sect. 2.4) may differ significantly from the pre-failure bond state. Here, an adjustment to the collision physics is developed in order to provide the user of the model greater control of where and how energy and momentum are dissipated within the system when cracks develop. This is done by considering the continuity of the elastic energy and the normal component of the force (as defined by bond physics) at the transition from bond to collision physics. An area of element overlap adjustment, A_o, can be incorporated into the expression for the collision force along with a durability parameter,

$$\mathbf{F}^{\mathbf{c}}_{\mathbf{elas}} = \gamma k_e^* D_c (A_i - A_o) b_w \hat{\mathbf{n}}. \tag{30}$$

Similarly, the elastic energy stored in the collision contact can be written as

$$W^c = \frac{D_c k_e^*}{\overline{s}} \frac{(A_i - A_o)^2}{2}. \tag{31}$$

Setting $A_o = A_i$ at the moment of failure emulates the situation in which the overlap area collapses at failure with all elastic energy immediately released. Setting $A_o = 0$ causes the force at the moment of failure to change by the difference $\mathbf{F}^{\mathbf{c}}_{\mathbf{elas}} - \mathbf{F}^{\mathbf{b}}_{\mathbf{elas}}$, and similarly for the energy. In order to offer a constraint on this transition, we consider the component of the normal bond force $F_\perp^b = \mathbf{F}^{\mathbf{b}}_{\mathbf{elas}} \cdot \mathbf{n_n}$ and the associated elastic bond energy $W_\perp^b$. We can seek solutions for A_o and D_c that specify the post-failure normal force to be some fraction α of the pre-failure force, and the post-failure elastic energy to be some fraction β of the pre-failure energy

$$\alpha F_\perp^b = \mathbf{F}^{\mathbf{c}}_{\mathbf{elas}} \cdot \mathbf{n_n}, \tag{32}$$

and

$$\beta W_\perp^b = W^c. \tag{33}$$

Using Eq. (30) and Eq. (31) to substitute into Eq. (32) and Eq. (33), A_o and D_c can be solved for in terms of the bond state at the time of failure

$$A_o = A_i - \frac{b_w \beta W_\perp^b}{\alpha F_\perp^b}, \tag{34}$$

and

$$D_c = \frac{\alpha F_\perp^b \overline{s}}{k_e^* b_w (A_i - A_o)}, \tag{35}$$

to conserve or reduce ($\alpha < 1, \beta < 1$) the force and energy of the contact through the transition. In some cases, the overlap adjustment A_o necessary to conserve both force and energy requires inflating the overlap area ($A_o < 0$) which is not feasible

https://doi.org/10.5194/egusphere-2026-4034
Preprint. Discussion started: 27 July 2026

(as the elements would remain in contact beyond the point when their polygons cease to overlap). Therefore, we primarily use these criteria to ensure that the post-failure normal force is set equal to $\alpha F_{\perp}^{b}$ and that the post-failure elastic energy be not greater than $\beta W_{\perp}^{b}$. In Sect. II-2.2.3 below, simple examples of force and energy being controlled through the bond to collision transition are presented.

3.4 Post-failure weakening

Situations can arise in simulations where elements with bonds that fail under compression continue to be stressed into configurations with very large element overlap. In extreme situations, the centroid of one element can pass over the centroid of another, causing a rapid reversal in the direction of force between the two. It is both physically reasonable and numerically justifiable to assume that the ice that constitutes the overlap between the elements in these situations becomes crushed or fails out-of-plane. To account for this, contact stiffness is allowed to continue to degrade post-failure under large enough compressive stress, analogous to how element bond weakening occurs.

$$\frac{dD_c}{dt} = \begin{cases} 0 & \text{for } \sigma_n < \tilde{\sigma_c} \quad \textit{no further collision damage}, \\ -f_{rc}\frac{\sigma_t}{\sigma_c} & \text{for } \sigma_n > \tilde{\sigma_c} \quad \textit{compressive collision failure}, \end{cases} \tag{36}$$

where $f_{rc} = \Gamma f_r$, with Γ being a tunable parameter. Once D_c drops below a minimum threshold, D_t, the material is considered to have only residual strength. At this point, A_o is set equal to A_i each time the maximum compressive strength is exceeded, allowing elements to fail further without more reduction in elastic properties.

4 Model implementation

4.1 Spherical Coordinates

The model is formulated in spherical coordinates in order to better represent basin and planetary scales with less distortion than would be offered with a Cartesian projection. For each model element, the three components of the angular acceleration vector on the surface of the sphere $\boldsymbol{H}$ are solved for as

$$\boldsymbol{H} = \dot{\boldsymbol{\Omega}} = \left(-\frac{F_y}{mR}, \frac{F_x}{mR}, \frac{N}{I}\right)^T, \tag{37}$$

in a coordinate frame centered on the element centroid, such that the local x- and y- directions form a tangent plane at that point. Here Ω is the element-local angular velocity, $\dot{\Omega} = d\Omega/dt$, F_x and F_y are the total forces on an element centroid in the local x- and y- directions, N is the torque normal to the x-y plane, I is the moment of inertia about the radial axis that extends from the center of the sphere to the element centroid, m is element mass and R is the radius of the sphere. Currently, only the contact forces on the element edges contribute to N. The radius of the sphere may be varied to represent different planets.

https://doi.org/10.5194/egusphere-2026-4034
Preprint. Discussion started: 27 July 2026

4.1.1 Using quaternions for element position and orientation

The motion of discrete polygons confined to the surface of a sphere is analogous to three-dimensional rigid body rotation about a fixed point. In essence, each element can be viewed as a pendulum with center of mass connected to the center of the sphere by a massless rod. With this perspective, a convenient and compact way to represent the position and orientation of each element is found in the mathematics of unit quaternions. Quaternions are an ordered set of four numbers that can describe position and orientation or rotations in a 3-dimensional space. Because of this, they have been used in fields such as computer graphics, robotics, and orbital mechanics. Several of the advantageous properties of unit quaternions include: 1) They can describe any three-dimensional rotation about an arbitrary axis uniquely, 2) every point on a sphere is treated exactly the same as any other point (no critical points), 3) The density of coordinate lines does not change from point to point, and 4) coordinate transformations and other operations can be performed compactly without involving trigonometry. In the model, a single quaternion is sufficient to uniquely describe the position and orientation of an ice element.

A distinct local coordinate system defines the relationship between the center of mass of each polygonal element and its vertices. But in order to easily relate the position of one element to another (for purposes of contact analysis) it is necessary that the quaternions that describe each element's orientation globally be defined consistently. In order to do this, the initial quaternion for each element is specified as the quaternion rotation that moves an oriented-vector from the north pole to the center-of-mass position and orientation of the element on the shortest (great circle) path. That is, if the center of mass of the element in the global reference frame is (c_x, c_y, c_z) and $\hat{e_z}$ is a unit vector directed from the center of the unit sphere to the north pole, then the initial quaternion (q_o) for each element can be specified as,

$$\mathbf{q_0} = \cos\frac{\theta}{2} + \hat{\mathbf{e}}\sin\frac{\theta}{2}, \tag{38}$$

where

$$\theta = \arccos\frac{c_z}{|\boldsymbol{c}|}, \tag{39}$$

and

$$\hat{\mathbf{e}} = \boldsymbol{c}\times\hat{e}_z/|\boldsymbol{c}\times\hat{e}_z|. \tag{40}$$

4.2 Element position update

Position update is performed in the model by numerically time-stepping the orientation quaternions associated with each element (Step 12 in Figure 1). In the global frame of reference, the update can be expressed in terms of the 3-dimensional angular velocity $\boldsymbol{\omega}$.

$$\dot{\mathbf{q}} = \frac{1}{2}\boldsymbol{\omega}\circ\mathbf{q}. \tag{41}$$

Where $\dot{q} = dq/dt$ and $\circ$ indicates quaternion multiplication. Contact forces are more easily determined in the element-local frame. So it is beneficial to express this in terms of the element-local angular velocity $\boldsymbol{\Omega}$. This can be done by using the

https://doi.org/10.5194/egusphere-2026-4034
Preprint. Discussion started: 27 July 2026

quaternion rule for translating between frames. That is if $\boldsymbol{A}$ is a vector in the global frame and $\boldsymbol{a}$ is one in the local frame, the orientation quaternion relates the two such that

$$\boldsymbol{A} = \bar{\mathbf{q}} \circ \boldsymbol{a} \circ \mathbf{q}, \qquad ,\boldsymbol{a} = \mathbf{q} \circ \boldsymbol{A} \circ \bar{\mathbf{q}}, \tag{42}$$

where $\bar{\mathbf{q}}$ is the complex conjugate of $\mathbf{q}$. Using this property, the expression for $\dot{\mathbf{q}}$ can be written as

$$\dot{\mathbf{q}} = \frac{1}{2}\mathbf{q} \circ \boldsymbol{\Omega}. \tag{43}$$

Position update proceeds once the forces and torques on the element $\boldsymbol{H}$ have been estimated, by first updating the local angular velocity at time step n, $\boldsymbol{\Omega}^n$ as

$$\boldsymbol{\Omega}^n = \boldsymbol{\Omega}^{n-1} + \Delta t\, \boldsymbol{H}^n, \tag{44}$$

where n indicates the current time step and $n-1$ the previous. All the forces $\boldsymbol{H}$ in this equation are approximated using forward Euler time-stepping (estimated from the current time step velocities and positions), except for the Coriolis term (Eq. (4)) for which an Adams-Bashforth time-stepping is used (estimated from a weighted average of current and previous timestep) due to it being unconditionally unstable with the Euler approach. Eq. (43) is numerically integrated forward in time using an Euler time step as well.

$$\mathbf{q}^{n+1} = \mathbf{q}^n + \frac{\Delta t}{2}\mathbf{q}^n \circ \boldsymbol{\Omega}^n. \tag{45}$$

More sophisticated time-stepping schemes may be considered in the future. It is recognized that this Euler time integration has limited accuracy not only because it provides only a first-order Taylor expansion of the derivative but also because it introduces an error that moves the quaternion off the unit circle. This is dealt with by re-normalizing the quaternion on each time step.

$$\overline{\mathbf{q}}^{n+1} = \frac{\mathbf{q}^{n+1}}{|\mathbf{q}^{n+1}|}. \tag{46}$$

This approximate correction can be inadequate for very large values of Ω, large elements relative to the size of the sphere, and/or large time steps, and a number of more accurate time stepping schemes have been determined in recent years. However, none of these concerns are particularly relevant to the simulation of sea ice at the scales being considered here, as the time stepping requirements for the contact physics are quite strict already.

4.3 Contact force frame of reference

The contact physics described above is based on interactions between polygons in a plane. But because the displacements at element contacts over a time step are extremely small, it is deemed reasonable to utilize the overlap between polygons in a two-dimensional tangential plane centered near the point of contact to estimate the surface forces on the sphere. This physical simplification provides computational efficiency, but requires mapping between the global spherical and local Cartesian frames associated with each element contact. For a given contact, the local 2-dimensional Cartesian coordinate utilizes the origin of

https://doi.org/10.5194/egusphere-2026-4034
Preprint. Discussion started: 27 July 2026

the centers of mass (e_1) of one of the contact elements as the point of contact for the tangential plane. The second element of the collision (e_2) is projected onto the local coordinate plane of the first element (e_1). In order to project e_2, the rotation matrix R that translates its local reference frame to that of e_1-local is first determined from the orientation quaternions of the two elements. This is achieved with computational efficiency (Eberly, 2008) using standard libraries, which involve fewer math operations than using the quaternions directly. Once the coordinates of the e_2 vertices in the e_1 reference frame are determined, the vertices positions of both elements are projected on a flat plane using a gnomonic projection and vertex displacements (for bonds) and overlap areas (for collisions) are calculated.

The gnomic projection is an azimuthal projection for which angles are preserved, but distance errors grow radially away from the origin of the coordinate system. The radial distance on the projection, r_g compared to the true distance from the origin r_o can be expressed as

$$\frac{dr_g}{dr_o} = \frac{1}{\cos^2 \frac{r_o}{R}}. \tag{47}$$

The transverse scale p_g on the gnomic projection also increases radially, but at a slower rate

$$\frac{dp_g}{dr_o} = \frac{1}{\cos \frac{r_o}{R}}. \tag{48}$$

Consequently, the farther a vertex is from the origin of e_1 in a contact, the larger the projection error. So, the error in estimating the forces at a contact will increase as element size increases relative to the planetary scale. Even so, as the vertices of the two contacting elements will be displaced similarly, the error in the distance between the vertices will be quite small. For example, if 1 m separates the position of the vertices of two elements in a contact located 100 km from the centroid of a very large element, the error in the displacement between the two would be less than 0.25 mm.

The contact force and contributions to torque calculated in the e_1 tangent plane act on the surface of the sphere at the centroid of e_1. The corresponding contributions to e_2 are determined by translating the equal but opposite two-dimensional force vector onto the e_2-plane using the transpose of R. Because the two tangent planes are not identically oriented, this produces a very small radial component to the translated force. In order to eliminate this without altering the magnitude of the force, the local in-plane components are augmented through a normalization factor

$$\xi = \sqrt{\frac{F_x^2 + F_y^2 + F_z^2}{F_x^2 + F_y^2}}.$$

5 Creating an initial element distribution

The model consists of discrete convex polygon elements, which have several advantages and costs compared to two-dimensional discrete element methods based on disks. One advantage of polygons is that they can fully fill a space to represent 100% ice coverage. They can also more directly match the shapes of sea ice floes observed in nature on scales of meters to kilometers. Matching the shapes means that interactions between floes are more naturally represented, where disk shaped elements, which contact each other along curved edges, must make special accommodations for rolling resistance. Relative costs of polygon-

https://doi.org/10.5194/egusphere-2026-4034
Preprint. Discussion started: 27 July 2026

based methods include the complexity of the contact physics, the arbitrariness of contact edge orientations, and the challenges in generating an initial distribution of elements to fill a particular domain.

A mostly automated method for generating the initial distribution is described. By automating the procedure, it is possible to create multiple randomized distributions of elements for a given domain, relatively quickly to produce ensemble sets to address the issue of sensitivity to initial element edge orientations on simulation outcome. We can use element size to focus computational expense to regions of interest or resolve small scale processes in a much larger domain. This is useful for example for ice-coast interaction, where details of the coastal or landfast ice edge shape may be critical, while allowing larger scale stress propagating through the regional or ocean wide ice pack is also vital.

Here, we use tools designed for two-dimensional polygons and finite element mesh generation and refinement. Initial element distributions are specified in a Cartesian plane to facilitate this. For a regional domain, an appropriate local map projection (e.g. an ESRI projection) can be used to map coastal boundaries onto the plane. Once the initial element distribution is generated, the inverse of the projection can be used to project all vertices onto the sphere. While this can lead to some distortion to the shape of the polygons, since vertices of adjacent polygons are collocated they will map to the same location on the sphere and not introduce erroneous initial contact forces.

For the case studies presented in this paper, we draw our domain boundaries based on coastlines from the Global Self-consistent Hierarchical, High-resolution Geography Database (Wessel and Smith, 2017) alternatively, a landfast ice edge can be used. Currently QuSI-DEM does not consider bathymetry nor temporal changes in ice thickness, so simulation of alteration to a landfast (grounded) ice edge is not feasible.

The procedure we use to generate the initial element distributions in complex domains generally follows the steps shown in Fig. 5. The methods used to generate grids are currently implemented in MATLAB but could be translated into other programming languages such as Python relatively easily. As all elements are represented as polygons, the first step in generating the initial distribution is to specify line-segment delineated boundaries marking the ice-covered regions. For each, an augmented region slightly larger than the ice-covered region is specified (Fig. 5a). This slightly larger region will be filled with elements, then elements that intersect the boundary of the region of ice cover are trimmed. This domain may contain islands, in which case additional polygons must be specified to identify the island coastline and a moderately smaller polygon shoreward of it for element-filling purposes. Finite element mesh generation tools are then used to fill the augmented regions with triangles using Delaunay triangulation. At this stage, mesh refinement may be used to specify enhanced resolution in desired regions or much lower resolution in others to balance the need for computational efficiency and the inclusion of far-field influences (Fig. 5b). The vertices determined from the triangulation in general will produce triangles that are close to equilateral, which, if tessellated, would produce a map of mostly hexagonal discrete elements. However, hexagonal elements can lead to anisotropy in the overall material behavior, as the mesh as a whole will be more susceptible to failure along preferred directions where rows of hexagonal elements align. To reduce the regularity of the grid, in general, the vertices output from the triangulation are randomly displaced by a fraction of their separation distance. Then a tessellation is performed to generate polygons from the 'perturbed' triangles to fill the prescribed augmented regions (Fig. 5c). The set of element-polygons thus created will fully fill the desired ice-covered region and overlap into the specified augmented regions. An automated procedure is then applied

https://doi.org/10.5194/egusphere-2026-4034
Preprint. Discussion started: 27 July 2026

to identify the elements intersecting the desired ice boundaries and clip, merge, reshape, and replace elements as necessary to exactly fill the region. This procedure allows us to achieve 100% ice coverage where desired in the model interior, as well as giving us control over the shape and behavior of the boundaries. For instance, ice can be initialized as bonded to the coast or free to slide along it without element corrugations playing a role in the behavior.

In order to form coastlines, a set of (immovable) coastal bounding (trapezoidal or triangular) elements with two vertices that match those of the elements along the domain edges are added to the set of elements (5d). The size of the boundary elements are scaled to be comparable or larger than that of the local interior elements where possible, to ensure that elements under high stress cannot pass through the coastal wall. Additional coastal walls may be added in ice free regions as well. The final step of the element generation process is to map the elements back onto the sphere, using the inverse of the mapping projection used to map the coastline to the plane (5e). All boundary elements are labeled based on the side of the original domain polygon on which they fall, so that different boundary conditions can be applied to each as appropriate.

An issue that can arise in this element generation procedure is that some (mostly edge elements) tend to be much smaller than their surrounding elements, or elements are produced in the clipping procedure near boundaries with extreme aspect ratios. These situations can greatly limit the time-step and cause unstable model behavior (if the small element becomes largely encompassed by a larger one). So, the algorithm includes checks for elements with these characteristics and where possible, merges them into the larger ones surrounding them, reshaping those surrounding elements when necessary to ensure convexity.

6 Summary

The Quaternion-based Sea Ice DEM (QuSI-DEM) is a build-out of a traditional polygon-based two-dimensional discrete element model for the simulation of sea ice. By formulating the model on a sphere, regional, basin, or even planetary-scale simulations can be undertaken. The model is presented here alongside a tool that allows for mesh refinement in the specification of the initial element distribution. This can alleviate the need for specification of open boundary conditions, as the domain can be extended far from the region of interest without excessive computational cost.

A polygon-based DEM has appeal for sea ice modeling because elements with distinct corners and linear sides bear more resemblance to typical pack ice floe geometry than disk-shaped elements. Issues with disk-shaped DEM models involving rolling resistance and packing arrangements are avoided, but the computational cost of polygon based approaches on a per element, or per contact basis tends to be higher. Additionally, challenges arise in matching the elastic characteristics of polygonal elements prior- and post-failure because of necessary differences in the way geometry is used to approximate forces and torques, as explained in Sect. 3. So efforts are made here to provide continuity in the model physics through the failure transition at contacts to avoid abrupt transitions in energy in the system that can be caused by numerical inconsistency. Crack propagation critically depends not only on bond failure but also on the post-failure characteristics of the material in the vicinity of the crack. So, the model also provides several mechanisms to control the weakening of both bond and collision contacts.

https://doi.org/10.5194/egusphere-2026-4034
Preprint. Discussion started: 27 July 2026

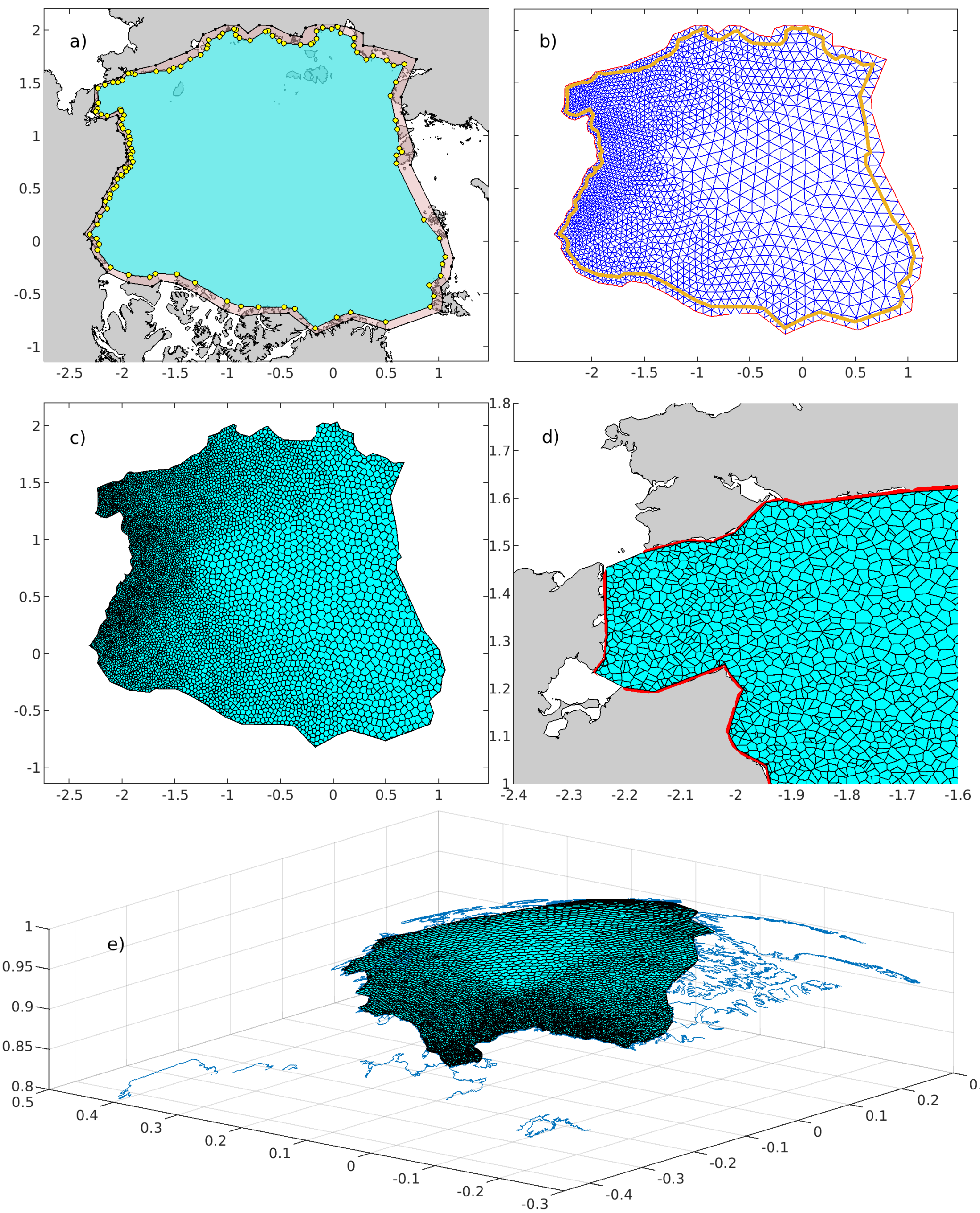

Figure 5. Process for generating the initial discrete element distribution for a coarse resolution Arctic Ocean setup. a) Specify domain polygon along with slightly larger encompassing polygon in a suitable map projection. b) Perform Delaunay triangulation on encompassing polygon. c) Perform Voronoi Tesselation and trim to domain polygon borders. d) Add edge-aligned boundary polygons at coastal boundaries. e) Transform coordinates onto a spherical surface.

https://doi.org/10.5194/egusphere-2026-4034
Preprint. Discussion started: 27 July 2026

In Part II of this manuscript, the basic QuSI-DEM functionality that has been introduced here is demonstrated and evaluated. Highly idealized simulations are used to explore failure characteristics, contact weakening and energy conservation at the level of a single, or small set of contacts. Realistic simulations of an ice arch at Bering Strait are utilized to demonstrate the impact various parameters can have on both qualitative and quantitative response of a system of many discrete elements. Sensitivity to the initial polygon distribution is tested by performing small ensembles of simulations for the Bering Sea ice arch sensitivity tests.

The goal of this modeling effort is to develop the ability to simulate sea ice dynamics with high local precision while allowing global force propagation through the pack. Such a model could be useful for targetted short term forecasting of sea ice drift, breakup and pressure. It is hoped that by being able to represent pre-failure stresses, failure mechanics and the post-failure physics of a granular assemblage the model may also be a useful tool for building rheologies appropriate for coarser resolution continuum sea ice models.

Code and data availability. The current version of QuSI-DEM is openly available from https://bitbucket.org/durskis/qusi-dem under the GNU General Public License, version 3.0 or later. The exact version used to produce the results in this paper is archived on Zenodo at https://doi.org/10.5281/zenodo.21367084 (Durski, 2026), together with the input data and run scripts needed to reproduce the simulations and figures presented in this paper. QuSI-DEM bundles the shapelib library (`deps/shapelib/`), which is distributed separately under its own GNU Lesser General Public License.

Author contributions. Conceptualization: SMD, JKH, and AK. Methodology and software: SMD, AB, AK, and GV. Validation: SMD and AB. Formal analysis, investigation, data curation, and visualization: SMD. Writing – original draft: SMD. Resources, supervision, and project administration: JKH. Writing – review & editing: JKH and AB. Funding acquisition: JKH and AK.

Competing interests. The authors declare that they have no competing interests.

https://doi.org/10.5194/egusphere-2026-4034
Preprint. Discussion started: 27 July 2026

References

Bažant, Z. P.: Scaling Laws for Sea Ice Fracture, in: IUTAM Symposium on Scaling Laws in Ice Mechanics and Ice Dynamics, edited by Dempsey, J. P. and Shen, H. H., pp. 195–206, Springer Netherlands, Dordrecht, ISBN 978-94-015-9735-7, https://doi.org/10.1007/978-94-015-9735-7_17, 2001.

Brenner, S., Horvat, C., Hall, P., Lo Piccolo, A., Fox-Kemper, B., Labbé, S., and Dansereau, V.: Scale-Dependent Air-Sea Exchange in the Polar Oceans: Floe-Floe and Floe-Flow Coupling in the Generation of Ice-Ocean Boundary Layer Turbulence, Geophysical Research Letters, 50, e2023GL105 703, https://doi.org/10.1029/2023GL105703, _eprint: https://agupubs.onlinelibrary.wiley.com/doi/pdf/10.1029/2023GL105703, 2023.

Chen, L. and Pei, Z.: Research on Fatigue Strength of Polar Icebreaker Structures Considering Ice Loads Based on Discrete Ice Element Model, Journal of Marine Science and Engineering, 13, 1545, https://doi.org/10.3390/jmse13081545, 2025.

Cundall, P. A. and Strack, O. D. L.: A discrete numerical model for granular assemblies, Géotechnique, 29, 47–65, https://doi.org/10.1680/geot.1979.29.1.47, 1979.

Dong, W., Chen, J., Zhang, Y., Wei, S., He, G., and Li, F.: Numerical Simulation of an Icebreaker Ramming the Ice Ridge, Journal of Marine Science and Engineering, 13, 1815, https://doi.org/10.3390/jmse13091815, 2025.

Durski, S. M.: QuSI-DEM: A polygon-based discrete element sea ice model in spherical coordinates, https://doi.org/10.5281/zenodo.21367084, software, 2026.

Eberly, D.: Rotation Representations and Performance Issues, Tech. rep., Geometric Tools, LLC, https://www.geometrictools.com/Documentation/RotationRepresentations.pdf, originally published 2002; last revised 2008, 2008.

Feng, Y. T., Han, K., and Owen, D. R. J.: Energy-conserving contact interaction models for arbitrarily shaped discrete elements, Computer Methods in Applied Mechanics and Engineering, 205-208, 169–177, https://doi.org/10.1016/j.cma.2011.02.010, 2012.

Herman, A.: Discrete-Element bonded-particle Sea Ice model DESIgn, version 1.3a – model description and implementation, Geoscientific Model Development, 9, 1219–1241, https://doi.org/10.5194/gmd-9-1219-2016, 2016.

Herman, A.: Wave-induced stress and breaking of sea ice in a coupled hydrodynamic discrete-element wave–ice model, The Cryosphere, 11, 2711–2725, https://doi.org/10.5194/tc-11-2711-2017, 2017.

Hibler, W. D. and Schulson, E. M.: On modeling the anisotropic failure and flow of flawed sea ice, Journal of Geophysical Research: Oceans, 105, 17 105–17 120, https://doi.org/10.1029/2000JC900045, _eprint: https://agupubs.onlinelibrary.wiley.com/doi/pdf/10.1029/2000JC900045, 2000.

Hopkins, M. A.: On the ridging of intact lead ice, Journal of Geophysical Research: Oceans, 99, 16 351–16 360, https://doi.org/10.1029/94JC00996, _eprint: https://agupubs.onlinelibrary.wiley.com/doi/pdf/10.1029/94JC00996, 1994.

Hopkins, M. A.: On the mesoscale interaction of lead ice and floes, Journal of Geophysical Research: Oceans, 101, 18 315–18 326, https://doi.org/10.1029/96JC01689, _eprint: https://agupubs.onlinelibrary.wiley.com/doi/pdf/10.1029/96JC01689, 1996.

Hopkins, M. A.: Using DEM to Model Arctic Sea Ice, in: Discrete Element Methods, pp. 374–379, American Society of Civil Engineers, https://doi.org/10.1061/40647(259)65, 2002.

Hopkins, M. A. and Thorndike, A. S.: Floe formation in Arctic sea ice, Journal of Geophysical Research: Oceans, 111, https://doi.org/10.1029/2005JC003352, _eprint: https://agupubs.onlinelibrary.wiley.com/doi/pdf/10.1029/2005JC003352, 2006.

https://doi.org/10.5194/egusphere-2026-4034
Preprint. Discussion started: 27 July 2026

Hopkins, M. A., Frankenstein, S., and Thorndike, A. S.: Formation of an aggregate scale in Arctic sea ice, Journal of Geophysical Research: Oceans, 109, https://doi.org/10.1029/2003JC001855, _eprint: https://agupubs.onlinelibrary.wiley.com/doi/pdf/10.1029/2003JC001855, 2004.

Khosravi, A., Sharifi, P., Durski, S. M., and Hutchings, J.: Discrete element simulations of granular sea ice in triaxial tests under different confining pressures and boundary conditions, Mechanics of Materials, 213, 105 567, https://doi.org/10.1016/j.mechmat.2025.105567, 2026.

Kulchitsky, A. V., Hutchings, J. K., Johnson, J. B., and Velikhovskiy, G.: Siku Discrete Element Method Sea Ice Model, in: Proceedings of the 23rd IAHR International Symposium on Ice, IAHR, Michigan, http://www.iahr.org/library/infor?pid=18475, 2016.

Lynmcnutt, S. and Overland, J.: Spatial hierarchy in Arctic sea ice dynamics, Tellus, 55, https://doi.org/10.3402/tellusa.v55i2.12088, 2003.

Moncada, R., Gupta, M., Thompson, A., and Andrade, J. E.: Level Set Discrete Element Method for modeling sea ice floes, Computer Methods in Applied Mechanics and Engineering, 406, 115 891, https://doi.org/10.1016/j.cma.2023.115891, 2023.

Moncada, R., Gupta, M., Ulloa, J., Thompson, A. F., and Andrade, J. E.: Simulating landfast sea ice breakage due to ocean eddies using a discrete element model, EGUsphere, pp. 1–24, https://doi.org/10.5194/egusphere-2025-3940, 2025.

Montemuro, B. P. and Manucharyan, G. E.: SubZero: a discrete element sea ice model that simulates floes as evolving concave polygons, Journal of Open Source Software, 8, 5039, https://doi.org/10.21105/joss.05039, 2023.

Tsarau, A., Lu, W., Lubbad, R., Løset, S., and Zhang, Y.: High-resolution regional sea-ice model based on the discrete element method with boundary conditions from a large-scale model for ice drift, Annals of Glaciology, 65, e25, https://doi.org/10.1017/aog.2024.26, 2024.

Turner, A. K., Peterson, K. J., and Bolintineanu, D.: Geometric remapping of particle distributions in the Discrete Element Model for Sea Ice (DEMSI v0.0), Geoscientific Model Development, 15, 1953–1970, https://doi.org/10.5194/gmd-15-1953-2022, 2022.

Wessel, P. and Smith, W. H. F.: GSHHG: Global Self-consistent Hierarchical High-resolution Geography, https://doi.org/10.5281/zenodo.7007502, 2017.

West, B., O'Connor, D., Parno, M., Krackow, M., and Polashenski, C.: Bonded Discrete Element Simulations of Sea Ice With Non-Local Failure: Applications to Nares Strait, Journal of Advances in Modeling Earth Systems, 14, e2021MS002 614, https://doi.org/10.1029/2021MS002614, _eprint: https://agupubs.onlinelibrary.wiley.com/doi/pdf/10.1029/2021MS002614, 2022.

Wilchinsky, A. V. and Feltham, D. L.: Modeling Coulombic failure of sea ice with leads, Journal of Geophysical Research: Oceans, 116, https://doi.org/10.1029/2011JC007071, _eprint: https://agupubs.onlinelibrary.wiley.com/doi/pdf/10.1029/2011JC007071, 2011.

Åström, J. A. and Polojärvi, A.: High-Resolution Fracture Dynamics Simulation of Pack-Ice and Drift-Ice Formation During Sea Ice Break up Events Using the HiDEM2.0 Code, Geophysical Research Letters, 51, e2024GL110 552, https://doi.org/10.1029/2024GL110552, _eprint: https://agupubs.onlinelibrary.wiley.com/doi/pdf/10.1029/2024GL110552, 2024.